Diffusion MRI of Complex Neural Architecture

Neurotechnique

David S. Tuch,[1,2,*] Timothy G. Reese,[1]
Mette R. Wiegell,[1] and Van J. Wedeen[1]
[1]Athinoula A. Martinos Center for Biomedical
   Imaging
Massachusetts General Hospital
149 13th Street, Room 2301
Charlestown, Massachusetts 02129
[2]Harvard-MIT Division of Health Sciences and
   Technology
77 Massachusetts Avenue, Room E25-510
Cambridge, Massachusetts 02139

Summary

While functional brain imaging methods can locate the cortical regions subserving particular cognitive functions, the connectivity between the functional areas of the human brain remains poorly understood. Recently, investigators have proposed a method to image neural connectivity noninvasively using a magnetic resonance imaging method called diffusion tensor imaging (DTI). DTI measures the molecular diffusion of water along neural pathways. Accurate reconstruction of neural connectivity patterns from DTI has been hindered, however, by the inability of DTI to resolve more than a single axon direction within each imaging voxel. Here, we present a novel magnetic resonance imaging technique that can resolve multiple axon directions within a single voxel. The technique, called q-ball imaging, can resolve intravoxel white matter fiber crossing as well as white matter insertions into cortex. The ability of q-ball imaging to resolve complex intravoxel fiber architecture eliminates a key obstacle to mapping neural connectivity in the human brain noninvasively.

Introduction

The connectivity of the nonhuman primate brain is well understood on the basis of an extensive body of tracer experiments. In contrast, the connectivity of the human brain remains poorly understood. The poor state of knowledge on the connectivity anatomy of the human brain is largely due to the lack of a method for measuring neural connectivity noninvasively. The development of a noninvasive imaging modality capable of measuring neural connectivity in vivo would provide invaluable information on how human cerebral cortex communicates and integrates information across disparate processing areas. Development of a noninvasive connectivity imaging method would also enable clinical diagnosis of connectivity disorders on an individual subject basis. Here, we present a novel diffusion-weighted magnetic resonance imaging (MRI) method called q-ball imaging that promises to significantly facilitate noninvasive mea-

*Correspondence: dtuch@mit.edu

surement of neural connectivity in the human brain in vivo.

Over the past few years, investigators (Basser et al., 2000; Conturo et al., 1999; Jones et al., 1999; Koch et al., 2002; Mangin et al., 2002; Mori et al., 1999; Mori and Van Zijl, 2002; Parker et al., 2002; Pierpaoli et al., 2001; Poupon et al., 2000; Xue et al., 1999) have proposed a method to measure neural connectivity noninvasively using a MRI technique called diffusion tensor imaging (DTI) (Basser et al., 1994b; Pierpaoli et al., 1996; Reese et al., 1995). DTI measures the molecular diffusion, that is, the random thermal motion, of the endogenous water in brain tissue. The reconstruction of neural connectivity patterns from DTI is based on the phenomenon of diffusion anisotropy in nerve tissue: water molecules diffuse relatively freely along the neural fiber direction but are hindered in the fiber-transverse direction. The hindrance of water diffusion in white matter is putatively due to the diffusion barrier presented by the cell membrane and the myelin sheath (Beaulieu, 2002; Le Bihan et al., 1993; Norris, 2001).

By measuring the direction of the diffusion anisotropy within each voxel, DTI provides an estimate of the neural fiber direction within each voxel. The resulting image represents a three-dimensional vector field image of the neural fiber orientation. The so-called tractography problem entails computationally reconstructing neural pathways from the diffusion tensor vector field (Basser et al., 2000; Conturo et al., 1999; Jones et al., 1999; Koch et al., 2002; Mangin et al., 2002; Mori et al., 1999; Mori and Van Zijl, 2002; Parker et al., 2002; Pierpaoli et al., 2001; Poupon et al., 2000; Xue et al., 1999). The tractography problem is analogous to the problem in hydrodynamics of reconstructing flow streamlines from a fluid-flow vector field.

Reconstruction of neural pathways from DTI is confounded, however, by the limitation that DTI can only resolve a single fiber direction within each voxel (Basser et al., 2000; Pierpaoli et al., 2001; Poupon et al., 2000; Wiegell et al., 2000). At the millimeter scale of the MR voxel, there is typically a distribution of fiber orientations within each voxel. For example, intravoxel orientational heterogeneity may arise from intersections between white matter bundles as well as the complex arrangement of fiber orientations at the cortical surface.

If there are multiple fiber orientations within a voxel due to, for example, fibers crossing or diverging within the voxel, DTI will estimate the fiber orientation to be the mean of the underlying fiber directions. The mean direction will not be representative of the true fiber directions, however. To consider an example, if one fiber points vertically and another fiber points horizontally, then the mean fiber direction will point toward the diagonal, differing from either of the underlying fiber directions. The inability to resolve multiple intravoxel fiber directions with DTI represents a substantial barrier to accurate mapping of white matter connectivity (Basser et al., 2000; Pierpaoli et al., 2001; Poupon et al., 2000; Wiegell et al., 2000).

The inability of DTI to resolve multiple fiber directions

stems from the assumption of Gaussian diffusion inherent to the tensor model (Alexander et al., 2002; Basser et al., 2000; Frank, 2001; Tuch et al., 2002). The tensor model assumes Gaussian diffusion, and a Gaussian function has only a single directional maximum. Consequently, the tensor model cannot capture multidirectional diffusion. Recently, it has been shown that in brain regions containing fiber crossing, the MR diffusion signal has significant multimodal structure, in clear disagreement with the tensor model (Tuch et al., 2002).

In an effort to resolve the fiber-crossing confound in DTI, investigators have introduced more elaborate models of the diffusion process in neural tissue (Alexander et al., 2002; Frank, 2001, 2002; Tuch et al., 2002). However, the model-based approaches require a number of assumptions. The mixture modeling approach, for example, assumes that each fiber population contains Gaussian diffusion and that there is no water exchange between fiber populations (Alexander et al., 2002; Tuch et al., 2002).

The fiber-crossing confound can also be resolved by imaging the diffusion function directly without a presumed model for the underlying diffusion process. A model-independent approach would not need to assume a single diffusion direction and would therefore be able to detect possible fiber-crossing structure. The diffusion function can be imaged model independently using so-called q-space methods such as q-space imaging (Callaghan, 1993; Callaghan et al., 1988; Cory and Garroway, 1990; Stejskal and Tanner, 1965) or diffusion spectrum imaging (DSI) (Tuch, 2002). Q-space imaging methods measure the microscopic diffusion function directly without any assumptions on the form of the underlying diffusion function.

With q-space imaging methods, it is possible to directly measure the microscopic three-dimensional diffusion function within each voxel of the MR image. The diffusion function, which we denote $P(\mathbf{r})$, describes the probability for a water molecule to undergo a displacement $\mathbf{r}$ in the experimental diffusion time τ (Callaghan, 1993; Cory and Garroway, 1990; Kärger and Heink, 1983). Q-space imaging methods are based on the Fourier relationship between the diffusion function $P(\mathbf{r})$ and the diffusion MR signal $E(\mathbf{q})$, a relationship that was first noted by Stejskal (Stejskal and Tanner, 1965). The Fourier relationship can be written explicitly as $P(\mathbf{r}) = F[E(\mathbf{q})]$, where F is the Fourier transform (FT) with respect to the experimental diffusion wavevector $\mathbf{q} = \gamma\delta\mathbf{g}$, γ is the nuclear gyromagnetic ratio for water protons, $\mathbf{g}$ is the diffusion-encoding magnetic field gradient, and δ is the duration of the gradient (Callaghan, 1993; Cory and Garroway, 1990; Stejskal and Tanner, 1965). Based on the Fourier relationship between the diffusion function and the diffusion MR signal, the diffusion function can be directly reconstructed by Fourier transform of the diffusion signal.

Q-space imaging methods are model independent and are therefore suitable for diffusion imaging of complex materials that may not exhibit simple unimodal diffusion. The technique has been applied extensively to characterize the microstructure of complex inanimate materials (Callaghan, 1999), biological tissue in vitro (Assaf and Cohen, 1999, 2000; Assaf et al., 2000; Kuchel et al., 2000), and small animals in vivo (King et al., 1994,

1997). Additionally, one-dimensional q-space imaging has been applied in humans in vivo (Assaf et al., 2002). In one-dimensional q-space imaging, the diffusion function is measured only along a single spatial dimension.

Using DSI, a variant of q-space imaging, we have recently obtained direct measurements of the three-dimensional diffusion function in the human brain in vivo (Tuch, 2002). By measuring the diffusion function directly without the constraints of the tensor model constraints, we have shown that is it is possible to resolve complex intravoxel tissue structure including intravoxel fiber crossing (Tuch, 2002). Further, measuring the microscopic diffusion function directly provides a model-independent picture of the underlying diffusion process.

By measuring the diffusion function directly, DSI can resolve multiple fiber directions within a single voxel and therefore eliminates the fiber-crossing confound in diffusion imaging. However, measuring the complete three-dimensional diffusion function requires long acquisition times and strong magnetic field gradients. The long acquisition times and gradient hardware demands have limited the routine implementation of q-space imaging methods, such as diffusion spectrum imaging, on conventional MR scanners. The key challenge has therefore been to devise an MR method that can resolve complex structure but is also practical for routine investigative purposes.

Here, we present a novel diffusion imaging method capable of resolving complex, subvoxel neural architecture. The imaging method is based on the Funk-Radon transform reconstruction, also known as the spherical Radon transform (Funk, 1916; Helgason, 1999). In a reference to q-space imaging, the technique is called q-ball imaging (QBI). The QBI technique is model independent and considerably more time-efficient than current q-space imaging methods. The efficiency gain is achieved by selectively measuring the angular structure of the diffusion function. By selectively measuring the angular structure of the diffusion function, it is still possible to resolve complex structure, yet the acquisition time is significantly reduced and the demands on the magnetic field gradients are also substantially reduced (Alexander et al., 2002; Frank, 2001; Tuch et al., 2002). The boost in sampling efficiency stems from the need to sample the diffusion signal only on a spherical shell as opposed to a complete three-dimensional Cartesian grid. The reduced gradient requirements follow from the need to sample only a single spatial frequency, i.e., the radius of the sampling sphere, instead of exhaustively sampling the high spatial frequencies necessary to satisfy the Nyquist condition. While the three-dimensional diffusion function provides invaluable information on the tissue microstructure, for the purposes of mapping neural fiber orientation, the angular structure of the diffusion function can capture much of the salient contrast.

"Angular structure" specifically means the radial projection of the diffusion function, that is, the function obtained by integrating the diffusion function over the radial dimension. We refer to the resulting spherical function as the diffusion orientation distribution function (ODF). The diffusion ODF is defined specifically as

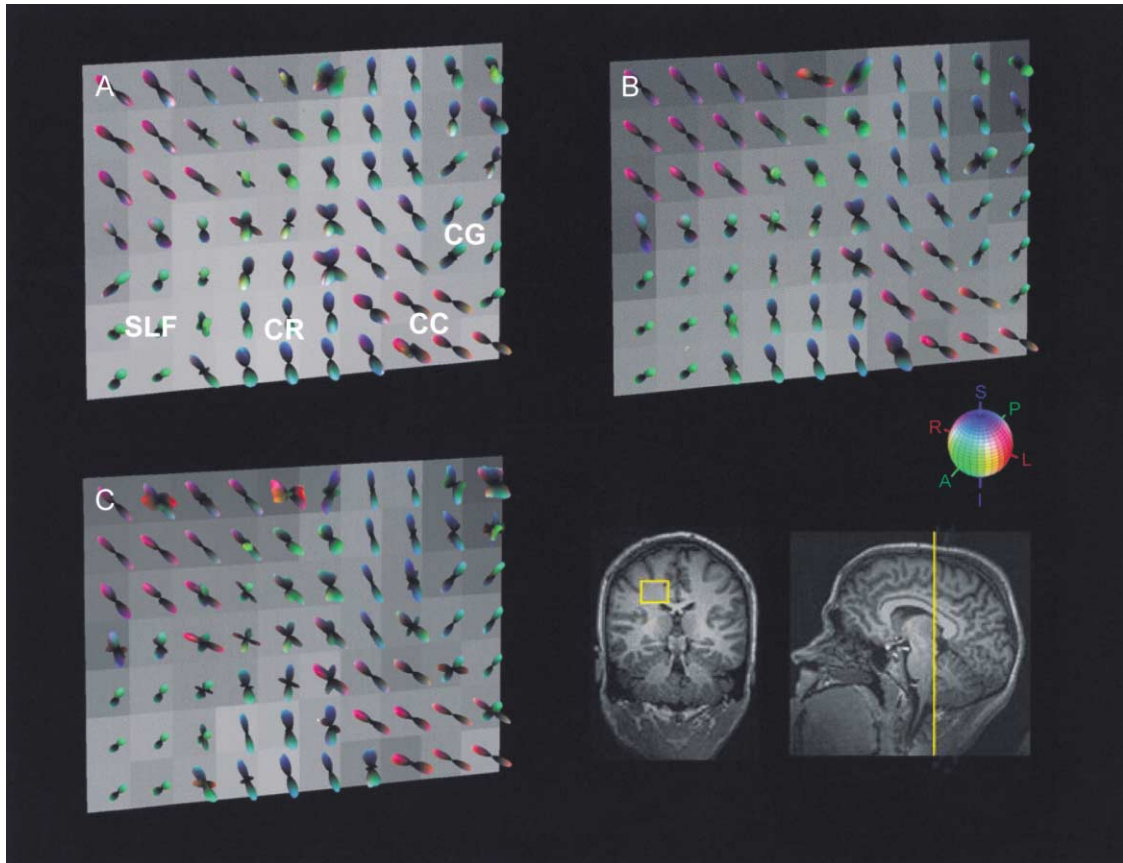$$\psi(\mathbf{u}) = \int_0^\infty P(r\mathbf{u})dr,$$

Figure 1. Diffusion ODF Maps of a Three-Way Fiber Crossing at the Callosal Striations

Coronal ODF maps from (A) DSI at $q_{max} = 1050$ cm^{-1}, $b_{max} = 1.7 \times 10^4$ s/mm^2; (B) QBI at $q = 670$ cm^{-1}, $b = 4 \times 10^3$ s/mm^2; and (C) QBI at $q = 950$ cm^{-1}, $b = 1.2 \times 10^4$ s/mm^2. The region of interest and anteroposterior level are shown in the structural images at bottom right. The region includes the intersection of the CR (blue) with the projections from CC (red). The ODF for each voxel is depicted as a color-coded spherical polar plot. For visualization purposes, each ODF has been min-max normalized. The ODFs are color-coded according to the red-green-blue color sphere shown at right, with red indicating medial-lateral, green showing anterior-posterior, and blue showing superior-inferior (Douek et al., 1991). The brightness is scaled by the ODF amplitude. The color channel mapping is $(red, green, blue)^T = \psi(\mathbf{u})|\mathbf{u}|$. Note how voxels containing a single fiber orientation such as the corpus callosum exhibit unimodal diffusion. In contrast, voxels containing intersecting fibers such as between the callosal projections and the corona radiata exhibit multimodal diffusion. Abbreviations: CC, corpus callosum; CR, corona radiata; CG, cingulate gyrus; SLF, superior longitudinal fasciculus.

where $\mathbf{u}$ is a unit direction vector and describes the probability for a water molecule to diffuse any distance in the direction $\mathbf{u}$ in the experimental diffusion time τ.

To understand the radial projection, it is helpful to think of the following analogy. The radial projection is comparable to projecting the three-dimensional distribution of stars onto the celestial sphere; information on the distance to the stars is lost, but the angular distribution of the stars is still retained. The ODF captures the relevant angular contrast of the diffusion function and, unlike the diffusion tensor, is capable of describing multimodal diffusion. In particular, the ODF can describe the complex diffusion patterns that arise from intravoxel fiber crossing. We show that the QBI technique can resolve complex subvoxel histoarchitecture including white matter fiber crossing and divergence within individual imaging voxels. Further, by varying the magnitude of the applied diffusion-sensitizing magnetic field gradient, it is possible to sensitize the diffusion signal to length scales on the order of tens of microns.

Results and Discussion

Diffusion MRI of Intravoxel Fiber Crossing

In regions of anatomic fiber crossing, both DSI and QBI resolved fiber-crossing structure within individual voxels. Figure 1 compares DSI (Figure 1A) with low spatial frequency (Figure 1B) and high spatial frequency (Figure 1C) QBI. The region of interest is taken from the three-way crossing between the corona radiata, the superior longitudinal fasciculus, and the striations of the corpus callosum. The color-coded orbitals depict the diffusion orientation distribution function (ODF). Multimodal ODFs, that is, ODFs with multiple peaks, indicate the presence of multiple fiber orientations within that voxel.

Multimodal ODFs are seen where the projections from the corpus callosum intersect the superior longitudinal fasciculus and where the projections from the corpus callosum intersect the corona radiata. Unimodal diffusion is seen in voxels where the fibers are homogeneously aligned within a voxel, such as in the body of
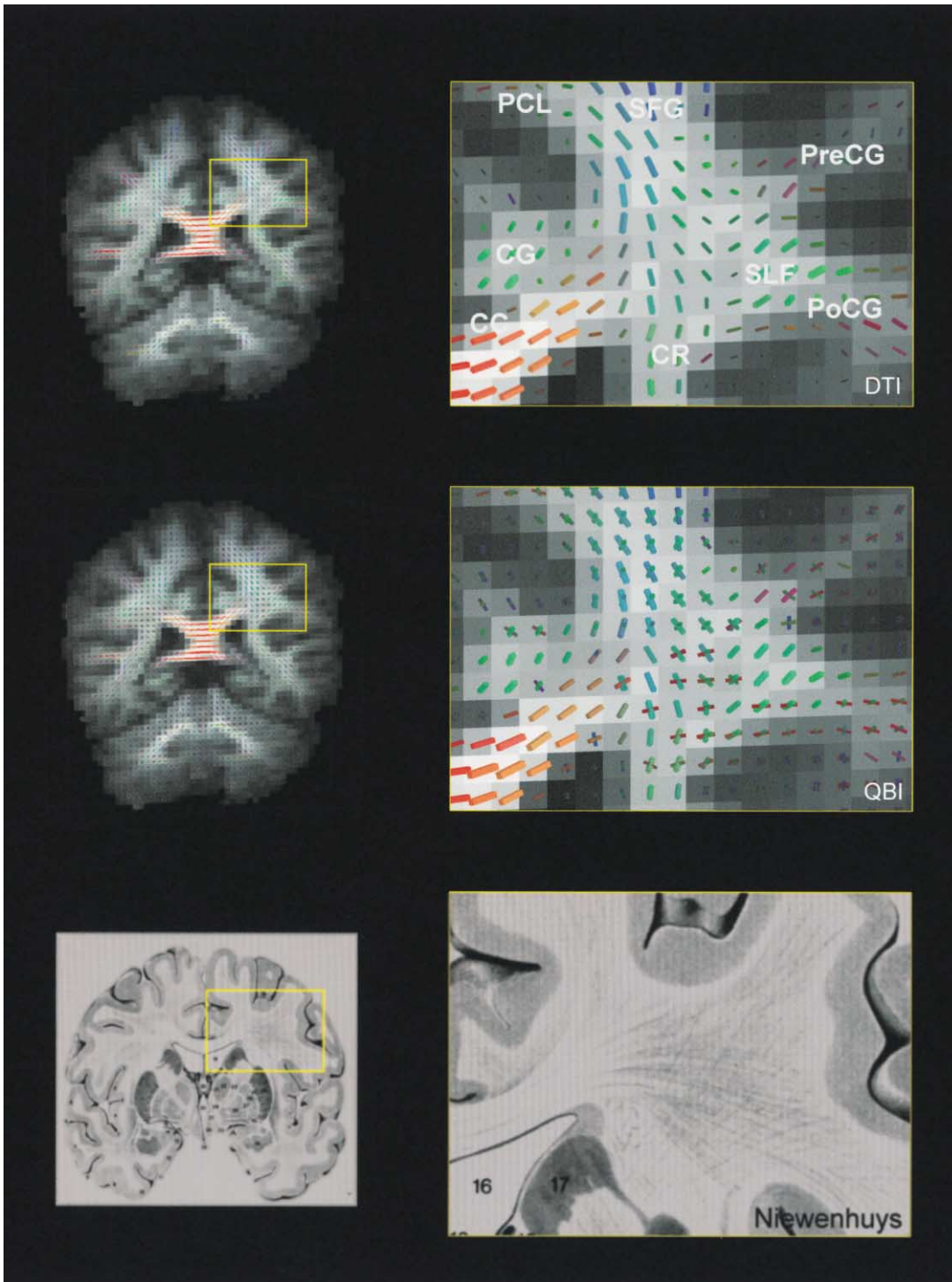
Figure 2. Comparison of DTI, QBI, and Nieuwenhuys Atlas

Comparison of DTI (top row), low-frequency QBI ($q = 670$ cm^{-1}) (middle row), and a histological tracing (bottom row) from the Niewenhuys atlas (Niewenhuys, 1996). The Niewenhuys tracing is taken from approximately the same level as the MRI. The DTI map is rendered as a cuboid field, where each cuboid is oriented in the direction of the principal eigenvector of the diffusion tensor within that voxel. The QBI map is rendered as multicuboid field where the cuboids represent the peaks of the ODF within that voxel. The cuboids are color-coded according to the red-green-blue scheme described in Figure 1 and are scaled by the fractional anisotropy for the DTI map and by the generalized fractional anisotropy for the QBI map.

The region-of-interest images (right column) are taken from the three-way intersection between the CR, SLF, and projections from the CC. At the intersection, DTI only shows the CR, whereas the QBI resolves the crossing between the CC, CR, and SLF. The intersection is shown in more detail in Figure 3. The projections of the SLF can be seen to extend as far superior as the level of the PCL. Also, the SLF intersects the projections to SFG. The fanning projections from the CC to PreCG and PoCG are clearly resolved. This fanning pattern is consistent within the histological results shown in the Niewenhuys figure (bottom row). In contrast, on the DTI (top row) the striations of the CC are obscured by the ascending CR. In the absence of the CC projections, PreCG and PoCG appear to receive no inputs. Abbreviations: CC, corpus callosum; CR, corona radiata; CG, cingulate gyrus; SLF, superior longitudinal fasciculus; PCL, paracentral lobule; PoCG, postcentral gyrus; PreCG, precentral gyrus; SFG, superior frontal gyrus.
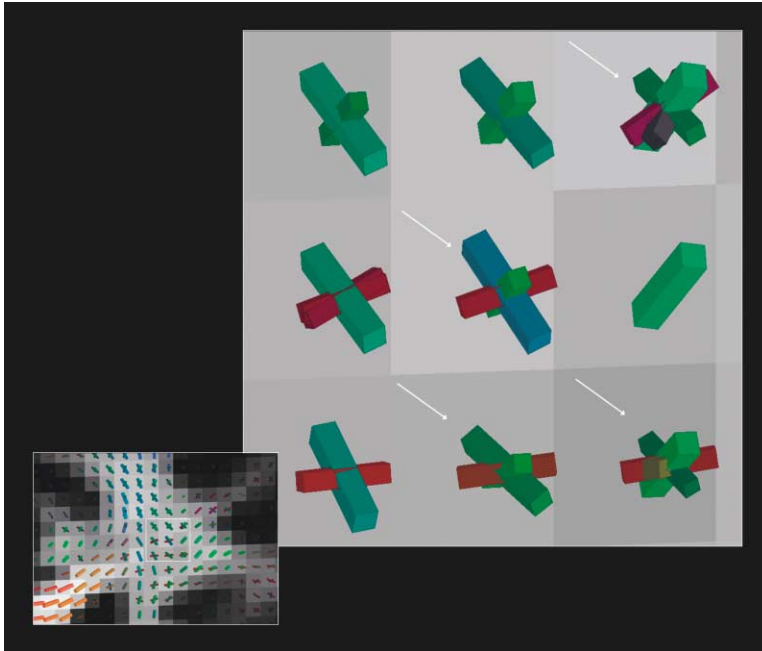
Figure 3. Magnified View of Three-Way Fiber Crossing at the Callosal Striations

White arrows point to voxels containing all three fiber populations. The red fibers directed inferior-medial to superior-lateral are the CC projections, the green fibers directed anterior-posterior are the SLF, and the green/ blue-green fibers directed inferior-lateral to superior-medial are the CR projecting to the SFG. Abbreviations: CC, corpus callosum; CR, corona radiata; SLF, superior longitudinal fasciculus; SFG, superior frontal gyrus.

the corpus callosum and in the corona radiata inferior to the intersection with the striations from the corpus callosum.

The high-frequency QBI (Figure 1C) revealed additional anatomical structure that was not evident on either the DSI or the low-frequency QBI. Specifically, in the high-frequency QBI (Figure 1C), the callosal striations interdigitate the corona radiata over a wider area and exhibit a more uniform density compared to the sparse appearance of the intersections in the DSI and low-frequency QBI. The interdigitation of the corpus callosum and the cingulate gyrus (green) is clearly resolved in the high-frequency q-ball image. The diffusion peaks for the high-frequency QBI were also sharper than those of the low-frequency QBI or DSI.

Comparison of Diffusion Tensor Imaging and Q-Ball Imaging

Figure 2 compares DTI with low-frequency QBI. The DTI and QBI were reconstructed from the same acquisition. As in Figure 1, the region of interest is taken from the intersection between the superior longitudinal fasciculus, the corona radiata, and the striations from the corpus callosum. For comparison, we also show a histological tracing from the Niewenhuys atlas (Niewenhuys, 1996). The Niewenhuys figure is from approximately the same anatomical level as the MRI slice.

Comparing the DTI and the QBI, we observe that on the DTI (Figure 2, top row), only the corona radiata is apparent. In contrast, the QBI shows the three-way crossing between the ascending projections of the corona radiata, the superior longitudinal fasciculus, and the striations of the corpus callosum. On the QBI, the callosal striations diverge to project to the precentral and postcentral gyrus, consistent with the Niewenhuys description (Figure 2, bottom row). On the DTI, the callosal striations as well as the superior longitudinal fasciculus are obscured by the corona radiata. The dominance of the corona radiata over the callosal projections and the superior longitudinal fasciculus on the DTI is likely due to the higher anisotropy of the corona radiata bundle.

The callosal striations are not observable on the DTI, and consequently the callosal fibers appear to project only to the superior frontal gyrus, which is inconsistent with Niewenhuys. Additionally, the precentral and postcentral gyri appear to have no connections. Further, the superior longitudinal fasciculus is obscured by the corona radiata and appears discontinuous. In contrast, QBI (Figure 2, middle row) resolved the striations of the corpus callosum to superior frontal gyrus, precentral gyrus, postcentral gyrus, and paracentral lobule, against the background of the corona radiata and superior longitudinal fasciculus projections. Note that the superior longitudinal fasciculus is not evident on the Niewenhuys section because the histological slice can only capture the in-plane fiber structure. The three-way crossing between the superior longitudinal fasciculus, the corpus callosum, and the projections from the corpus callosum is shown in more detail in Figure 3.

In the cingulate gyrus, QBI resolved the ascending projections to the superior lobe of the cingulate gyrus through the core anteroposterior-directed cingulum bundle. On the DTI, the ascending projections to the superior lobe of cingulate gyrus are not detectable. The minor anteroposterior-directed fibers seen in the superior lobe of the cingulate gyrus may be fibers from the main cingulum bundle.

Q-Ball Imaging of Intravoxel Composite Structure at Cortical Margin

In addition to resolving fiber crossing in deep white matter intersections, QBI was able to resolve composite
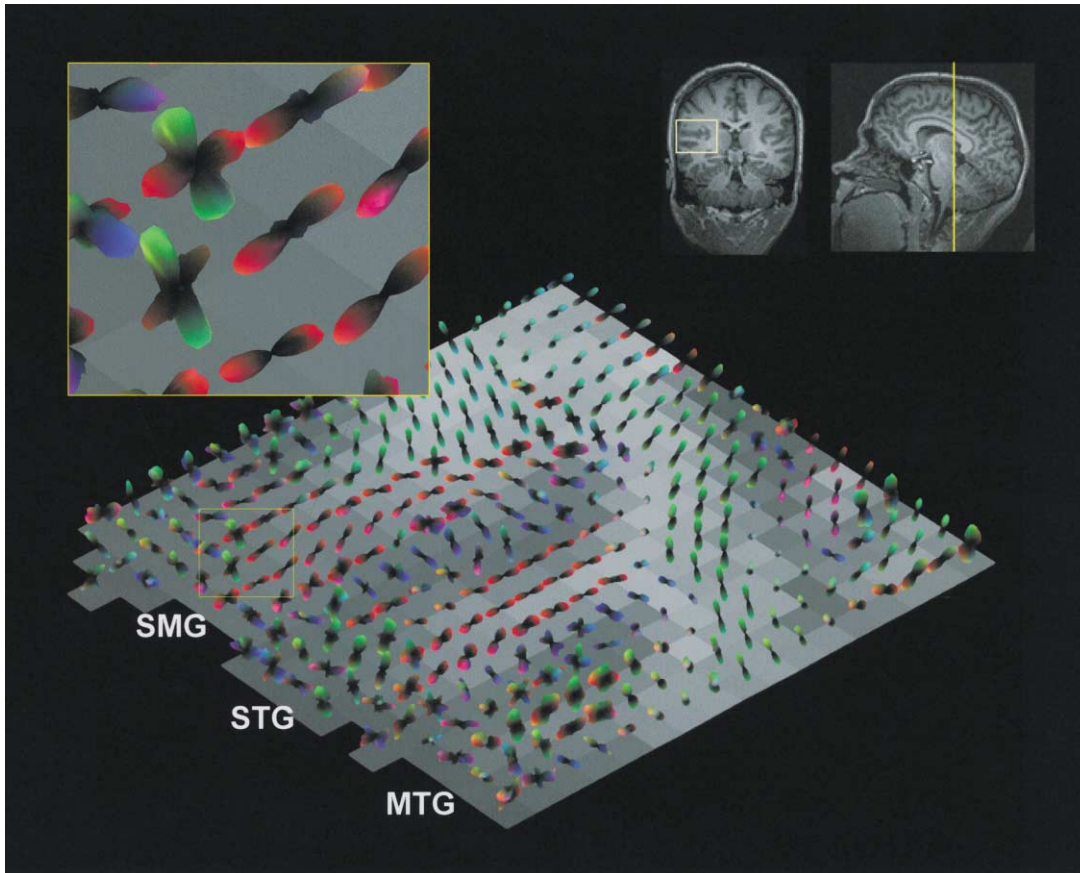
Figure 4. Coronal QBI Map of the Temporal Lobe

The map was generated from the sum of the low-frequency and high-frequency QBI acquisitions. The region of interest and anterior-posterior level are shown in the structural images at top right. The inset shown at top left (yellow box) shows apparent fiber crossing at the crown of SMG. Abbreviations: SMG, supramarginal gyrus; STG, superior temporal gyrus; MTG, medial temporal gyrus.

fiber architecture at the cortical margin. Figure 4 shows a coronal ODF map of the right temporal lobe. The map was generated from the mean of the low-frequency and high-frequency QBI.

Composite fiber structure is seen at the crown of the supramarginal gyrus (Figure 4, magnified region of interest) and to a lesser extent at the crown of the superior temporal gyrus. Complex structure is also observed along the walls of supramarginal gyrus and superior temporal gyrus. Along the gyral wall, the fiber directions are oriented approximately normal and parallel to the cortical surface. For both gyri, the surface-normal fiber component is oriented in the superior-inferior direction.

The anteroposterior mediolateral diffusion component reflects the insertion to the gyral crown. The antero-posterior diffusion component oriented normal to the cortical surface is attributed to the white matter insertions to cortex. The fibers bend rapidly, and therefore the curvature of the fibers cannot be resolved. The characteristic cross-hatched fiber structure at the gyral wall is also seen in the QBI in Figure 2 (middle row) in the cingulate gyrus and the precentral gyrus. The cross-hatched pattern is attributed to partial volume between the ascending projections to gyral crown and the inser-

tions to the gyral wall. Figure 5 provides a schematic illustration of this model.

Alternatively, the surface-normal diffusion component may be due to radially organized gray matter. This would be consistent with previous DTI reports of radial fiber architecture in rat cortex (Hoehn-Berlage et al., 1999), neonatal pig cortex (Thornton et al., 1997), and neonatal human cortex (McKinstry et al., 2002). Interestingly, McKinstry et al. (2002) reported that in neonatal human cortex, the radial fiber structure disappeared at gestational age 36 weeks. The disappearance of the radial fiber structure was attributed to the development of the basal, intracortical dendrites, which are oriented parallel to the cortical surface and obscure the radial structure. In DTI, composite fiber architecture in gray matter is undetectable because the tensor model incorrectly represents multimodal diffusion as isotropic diffusion.

To determine whether the surface-normal diffusion component originates from white matter or gray matter, it would be helpful to obtain QBI with high enough spatial resolution to resolve pure gray matter voxels. Another approach would be to measure an MR property of the surface-normal diffusion compartment, such as the T1 or T2 relaxation constant. Based on the measured pa-
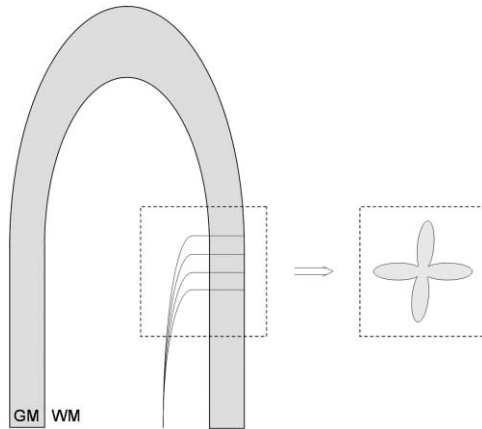
Figure 5. Schematic Model for the Cross-Fiber Architecture Observed along the Gyral Wall

The large arch depicts a gyrus, where the shaded region represents gray matter and the unshaded region represents white matter. The curves represent white matter fibers ascending the gyrus and then inserting into the gyral wall. The orbital shown at right depicts the diffusion ODF that would arise from the fiber geometry shown at left. The dashed box represents the voxel dimensions. The diffusion component oriented parallel to the cortical surface, i.e., vertical in the example, originates from the portion of the fibers ascending the gyrus. The diffusion component oriented normal to the cortical surface, i.e., horizontal in the example, is thought to arise from the white matter insertions to cortex. The cortical surface-normal diffusion component may also receive a contribution from radial gray matter architecture.

rameter, the surface-normal component could then be assigned to white matter or gray matter.

Limitations and Future Improvements

We have shown that q-ball imaging can resolve complex intravoxel white matter fiber structure, including fiber crossing in deep white matter and composite fiber structure at the cortical margin. The ability to resolve intravoxel fiber crossing will significantly benefit efforts to trace neural pathways with diffusion MRI. For example, the ability to resolve the intersection between the callosal striations and the corona radiata demonstrated in Figure 2 will allow for more accurate tractography of the callosal projections. Additionally, the resolution of the insertions into cortex will help track fibers to specific locations within a gyrus.

Numerous barriers still need to be surmounted, however, to obtain accurate tract reconstructions from diffusion imaging. Specifically, the exact relationship between the measured diffusion function and the underlying fiber geometry needs to be better understood. For example, QBI describes the fiber structure through the diffusion ODF, but there are multiple fiber arrangements consistent with a particular ODF. Consider an ODF with two peaks ($\times$). The underlying fiber structure may consist of crossing fibers ($\times$) or neighboring kinking fibers ($\rangle$ $\langle$), also called "kissing" fibers (Basser et al., 2000). Due to the reflection symmetry of the ODF, i.e., $\psi(\mathbf{u}) = \psi(-\mathbf{u})$, the fiber structure could also be a single bending fiber with one of four possible orientations ($\rangle$, $\langle$, $\wedge$, or $\vee$).

Characteristics of the ODF peaks themselves could

provide clues to distinguish these possibilities. In some cases, a crossing fiber arrangement can be distinguished from a kissing fiber pattern based on characteristics of the ODF peaks. For example, if one of the ODF peaks is significantly wider or longer than the other peak, then that would suggest a crossing fiber arrangement rather than a kissing fiber pattern. For a kissing fiber pattern, the ODF peaks would be more similar. Corresponding peaks can also be matched using other characteristics of the ODF peaks, such as MR relaxation properties including T2 or magnetization transfer. The ODFs from the neighboring voxels can also provide discriminating information. If an ODF peak at a particular voxel is consistent with the ODF peaks leading to and from that voxel, that would suggest that the peaks are connected.

For the purposes of connectivity reconstructions, it is essential to bear in mind that the measured diffusion ODF does not reflect the true fiber ODF. The tractography reconstructions would ideally be performed with the fiber ODF if it could be determined. In the streamline solutions commonly used in tensor-based tractography (Mori and Van Zijl, 2002), the fiber probability distribution is implicitly taken as a δ function around the principal eigenvector, i.e., $\psi_f = \delta(\mathbf{e}_1 - \mathbf{u})$. Developing a physically more accurate model of the fiber distribution would greatly improve the anatomical accuracy of tractography reconstructions.

The relationship between the diffusion ODF and the fiber ODF is governed by the diffusion physics and biophysical properties of the tissue such as the cell membrane permeability and the free diffusion coefficients for the cellular compartments. To the extent that the imaging physics and the diffusion properties of neural tissue are known, a forward model can be formulated to relate the fiber ODF to the diffusion ODF. Inverting the forward model would then give an estimate for the fiber ODF based on the measured diffusion ODF (Tuch et al., 2001). In addition to providing a more accurate estimate for the fiber distribution, solving for the fiber ODF would yield a sharper ODF since the dispersion effects of the diffusion process would be reduced or eliminated.

The ODF peaks can also be sharpened experimentally by tuning the diffusion wavevector to optimize the angular contrast-to-noise ratio. The optimal wavevector will depend on the diffusion characteristics of the tissue, including the diffusion anisotropy of the target fiber population and the angular separation of the individual populations. The optimal diffusion wavevector will also vary in neurodegenerative states that alter the diffusion environment.

Optimization of the sampling scheme may allow for significant improvements in the total acquisition time. We have implemented a research protocol that acquires a whole-head volume in approximately 35 min, by sampling 252 directions, corresponding to ~12° angular resolution. 252 sampling directions requires approximately the same acquisition time as a seven-direction DTI scan with 36 averages. Rather than a single sampling shell, the optimal sampling scheme may consist of multiple shells, each acquired with different wavevector. Multishell
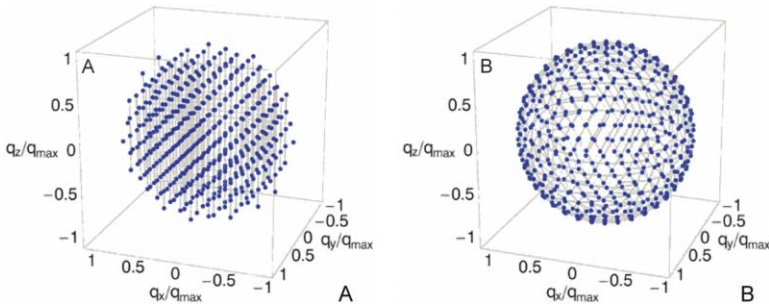
Figure 6. Q-Space Sampling Schemes for DSI and QBI Acquisitions

(A) The DSI sampling scheme (blue dots) is a spherically truncated Cartesian lattice. The spherically truncated lattice consists of the points (n = 515) on a 11 × 11 × 11 Cartesian lattice that lie within a sphere of diameter 11. (B) The QBI sampling scheme (blue dots) consists of the points (n = 492) obtained from the vertices of a 7-fold regularly tessellated icosahedron. The gray lattice is shown to facilitate visualization of the sampling scheme geometry.

sampling schemes can be analyzed straightforwardly with the mathematical framework described here.

DTI has been applied widely to map group effects related to changes in white matter microstructure (for reviews, see Kubicki et al., 2002; Lim and Helpern, 2002). Group statistics can also be calculated from the ODF maps based on either parameters derived from the ODF or on the whole ODF per se. The ODF group statistics can be calculated using tools developed for spherical statistics, which is a well-developed field of statistics (Fisher et al., 1987; Mardia and Jupp, 2000).

Relative to the diffusion tensor, the ODF offers a more complete and more accurate representation of the true diffusion function. ODF maps will therefore help in the interpretation of diffusion contrast, both at the individual and group levels. To cite one example, under the diffusion tensor model, neurodegeneration can lead to either a decrease or an increase in FA, depending on whether or not the region contains fiber crossing. The ODF can determine whether an observed reduction in anisotropy is due to a reduction in anisotropy in a single fiber population or increased orientational heterogeneity. Ultimately, the model independence and the resolving power of the ODF framework will help elucidate the fundamental biophysical mechanisms governing diffusion anisotropy in nerve tissue and provide a more accurate basis for inferring neural connectivity from diffusion-weighted imaging.

Experimental Procedures

Statement of the Problem
The basic problem is how to measure the angular structure of an object in Fourier space. In the context of the MR experiment, the MR diffusion signal E is related to the diffusion function P by the Fourier relation $P(\mathbf{r}) = F[|E(\mathbf{q})|]$, where $\mathbf{q}$ is the diffusion wavevector (Cory and Garroway, 1990; Stejskal and Tanner, 1965; Tuch, 2002). The orientational structure of the diffusion can be extracted from P by integrating over the radius of the function. The radial projection of the diffusion function is called the diffusion orientation distribution function (ODF) and is defined as

$$\psi(\mathbf{u}) = \int_0^\infty P(r\mathbf{u})dr,$$

where $\mathbf{u}$ is a unit direction vector. The ODF gives the probability for a spin to diffuse any distance in the direction $\mathbf{u}$ at the experimental diffusion time τ (Tuch, 2002). The ODF is a probability function defined on the sphere. The ODF is symmetric about reflection $\psi(\mathbf{u}) = \psi(-\mathbf{u})$ due to the reflection symmetry of the PDF, i.e., $P(\mathbf{r}) = P(-\mathbf{r})$, which in turn is a consequence of microscopic detailed balance.

The problem is then specifically the following: given $E(\mathbf{q})$ sampled on a sphere of radius q', how can one reconstruct the ODF? We show that one can obtain an approximation to the true ODF by computing the Funk-Radon transform (FRT) (Funk, 1916; Helgason,

1999) of the diffusion signal. The FRT is also referred to as the spherical radon transform.

Reconstruction Algorithm
The FRT, which we denote S, is an integral transform from the sphere to the sphere. The FRT is sometimes referred to as the spherical Radon transform or simply the Funk transform. Consider a function $p(\mathbf{w})$ on the sphere, where $\mathbf{w}$ is a unit direction vector. For a given direction of interest $\mathbf{u}$, the FRT is defined as the integral over the corresponding equator (Funk, 1916; Helgason, 1999):

$$S[p(\mathbf{w})] = \int_{\mathbf{w} \perp \mathbf{u}} p(\mathbf{w})d\mathbf{w}.$$

What is the relationship between FRT of the diffusion signal and the diffusion ODF? The relationship can be formulated most easily in cylindrical coordinates. The diffusion signal and the diffusion PDF are written in cylindrical coordinates as $E(q_r, q_\theta, q_z)$ and $P(r, \theta, z)$, respectively. Without loss of generality, let us take the direction of interest $\mathbf{u}$ to be the z direction. For a three-dimensional function, we can define the FRT as the FRT evaluated at a particular radius, say, q'. The FRT of E at a wavevector radius q' can be written in cylindrical coordinates as

$$S_{q'}[E] = \int E(q',q_\theta,0) \, dq_\theta = \int E(q_r,q_\theta,0)\delta(q_r\text{-}q')q_r \, dq_r dq_\theta dq_z. \quad (2)$$

Using Plancherel's theorem (Bracewell, 1999)

$$\int f(x)g^*(x) \, dx = \int F[f(x)]F^*[g(x)] \, dk \quad (3)$$

and the central slice theorem (Deans, 1993)

$$F[E(q_r,q_\theta,0)] = \int P(r,\theta,z)dz, \quad (4)$$

we then have (Tuch, 2002)

$$S_{q'}[E] = 2\pi q' \int P(r,\theta,z)J_0(2\pi q'r)r \, dr \, d\theta \, dz$$

$$= 2\pi q' \int H[P(r,\theta,z)] \, d\theta \, dz, \quad (5)$$

where we have used $F[\delta(q_r\text{-}q')] = 2\pi q' J_0(2\pi q'r)$, J_0 is the 0th order Bessel function, and H denotes the Hankel transform $H[f(r)] = \int f(r)J_0(2\pi kr)r \, dr$ (Arfken and Weber, 2000). Equation 5 can also be derived without Plancherel's theorem using a cylindrical wave expansion (Tuch, 2002). We note that Zavada and colleagues (Kimmich and Weber, 1993; Zavada and Kimmich, 1999; Zavada et al., 1999) derived a similar relation to Equation 5 for isotropic diffusion.

From Equation 5, we see that for a direction of interest z, the FRT of the diffusion signal is proportional to the mass of the Hankel transform of the PDF projected on the $r\theta$-plane. To the degree that the mass of J_0 is concentrated at the origin, the ODF obtained by FRT approximates the true ODF obtained by RP. If we replace the Bessel function in Equation 2 by a delta function, $\delta(r)$, then we obtain the RP exactly.

In summary, summing over a circle in Fourier space is approximately equal to summing the signal along the direction normal to the circle in real space. Due to the Fourier relationship between the diffusion MR signal and the diffusion function, we can exploit this finding to measure the diffusion probability in a particular direction by simply summing the diffusion MR signal along an equator around that direction.

The radius of the sampling sphere q' controls the width of the

Bessel function ($\sim 1/q'$), which in turn controls the angular resolution. Increasing q' sharpens the Bessel kernel and increases the ability to resolve distinct peaks. Less signal will pass through the projection kernel, however, and the signal-to-noise ratio will decrease. Conversely, decreasing q' widens the Bessel kernel and reduces the power to discriminate peaks but increases the signal-to-noise ratio. The sampling radius wavevector q' controls the tradeoff between the sharpness and the mass of the projection kernel, which determines the tradeoff between angular resolution and the signal-to-noise ratio.

Image Acquisition
Single-shot, echo-planar diffusion-weighted MR images of a healthy volunteer were acquired on a 3.0 T Siemens Allegra scanner (Erlangen, Germany) at the Massachusetts General Hospital NMR Center (Charlestown, MA) (Turner and Le Bihan, 1990). The study was performed with informed consent using a research protocol approved by the Massachusetts General Hospital Internal Review Board (IRB). Three experiments were performed: one diffusion spectrum imaging (DSI) acquisition with Cartesian sampling and two q-ball imaging (QBI) acquisitions with spherical shell sampling. All of the diffusion images were acquired using a twice-refocused spin echo pulse sequence ($90°-g_1-180°-g_2-g_3-180°-g_4-$acquire) (Reese et al., 2003). The 180-pulse pair was positioned to minimize image distortions due to eddy currents (Reese et al., 2003).

The slice prescription for all three acquisitions was identical. Two coronal slices (slice thickness, 2.8 mm; slice gap, 6.72 mm) were obtained using a 64×64 acquisition matrix and a 17.92×17.92 cm field-of-view, providing 2.8×2.8 mm in-plane voxel resolution. Whole-head, high-resolution structural images (3D MPRAGE) (Mugler and Brookeman, 1990) were also acquired for anatomical reference.

The DSI sequence parameters were TR/TE/δ = 800/143/61 ms, $b_{max} = 1.7 \times 10^4$ s/mm^2, $g_{max} = 40$ mT/m, and $q_{max} = 1050$ cm^{-1}. The q-space sampling scheme consisted of a spherically truncated Cartesian lattice, i.e., the points on a $N \times N \times N$ Cartesian lattice that lie within a sphere of diameter of N (Figure 6A). The lattice dimension was $N = 11$, giving n = 515 q-space sampling points. This encoding gives lattice width $2q_{max} = 2100$ cm^{-1}, lattice spacing $\Delta q = 2q_{max}/(N - 1) = 210$ cm^{-1}, spatial resolution $(2q_{max})^{-1} = 4.76$ μm, and FOV $(\Delta q)^{-1} = 47.69$ μm.

The two QBI acquisitions consisted of a "low-frequency" acquisition ($q = 670$ cm^{-1}, $b = 4 \times 10^3$ s/mm^2) and a "high-frequency" acquisition ($q = 950$ cm^{-1}, $b = 1.2 \times 10^4$ s/mm^2). A fourth data set was reconstructed from the average of the low-frequency and high-frequency q-ball imaging data sets. The q-space sampling points (n = 492) for both acquisitions were obtained from the vertices of a 7-fold tessellated icosahedron, which gives an angular resolution of 9.30° (Figure 6B). The sequence parameters for the first (low-frequency) QBI acquisition were TR/TE/δ = 800/98/39 ms, $b_{max} = 4.0 \times 10^3$ s/mm^2, $g_{max} = 40$ mT/m, and $q = 670$ cm^{-1}, giving FWHM = 7.22 μm for the Bessel projection kernel. The parameters for the second (high-frequency) QBI experiment were TR/TE/δ = 800/130/55 ms, $b_{max} = 1.2 \times 10^4$ s/mm^2, and $q = 950$ cm^{-1}, giving FWHM = 5.10 μm for the Bessel projection kernel.

Image Reconstruction
For the DSI acquisition, the ODF for each voxel was reconstructed by zero-filling the diffusion signal lattice and computing the fast FT and then the RP. The RP was calculated using cubic spline interpolation (de Boor, 2001) with $r_{max} = $ FOV/2 = 23.85 μm. The RP was evaluated for $m = 752$ directions, which were obtained from the vertices of a 5-fold tessellated dodecahedron. Each ODF was then normalized to unit mass.

For the QBI, the ODF was calculated for each voxel using the FRT:

$$\psi(\mathbf{u}) = \int_{\mathbf{q} \perp \mathbf{u}} E(\mathbf{q}) d\mathbf{q},$$

where $\mathbf{u}$ is the diffusion direction of interest. The ODF was evaluated for $m = 752$ directions corresponding to the vertices of a 5-fold tessellated dodecahedron. The FRT was computed using spherical radial basis function interpolation with a spherical Gaussian kernel ($\sigma = 12.0°$) (Fasshauer and Schumaker, 1998; Hardy and Nelson, 1986). The reconstructed ODFs were then smoothed with a spherical

Gaussian kernel ($\sigma = 13.2°$) and normalized to unit mass. The ODF peaks were defined as local maxima of the ODF with amplitude greater than the ODF mean for each voxel. For both the DSI and QBI acquisitions, the generalized fractional anisotropy (GFA) was calculated as GFA = std(ψ)/rms(ψ), where std is the standard deviation and rms is the root-mean-square. The diffusion tensor $\mathbf{D}$ was calculated for each voxel using a noise-whitened least-squares fit to the diffusion signal (Basser et al., 1994a).

References

Alexander, D.C., Barker, G.J., and Arridge, S.R. (2002). Detection and modeling of non-Gaussian apparent diffusion coefficient profiles in human brain data. Magn. Reson. Med. *48*, 331–340.

Arfken, G.B., and Weber, H.J. (2000). Mathematical Methods for Physicists, 5th edition (New York: Harcourt).

Assaf, Y., and Cohen, Y. (1999). Structural information in neuronal tissue as revealed by q-space diffusion NMR spectroscopy of metabolites in bovine optic nerve. NMR Biomed. *12*, 335–344.

Assaf, Y., and Cohen, Y. (2000). Assignment of the water slow-diffusing component in the central nervous system using q-space diffusion MRS: implications for fiber tract imaging. Magn. Reson. Med. *43*, 191–199.

Assaf, Y., Mayk, A., and Cohen, Y. (2000). Displacement imaging of spinal cord using q-space diffusion-weighted MRI. Magn. Reson. Med. *44*, 713–722.

Assaf, Y., Ben-Bashat, D., Chapman, J., Peled, S., Biton, I.E., Kafri, M., Segev, Y., Hendler, T., Korczyn, A.D., Graif, M., and Cohen, Y. (2002). High b-value q-space analyzed diffusion-weighted MRI: application to multiple sclerosis. Magn. Reson. Med. *47*, 115–126.

Basser, P.J., Mattiello, J., and LeBihan, D. (1994a). Estimation of the effective self-diffusion tensor from the NMR spin echo. J. Magn. Reson. B. *103*, 247–254.

Basser, P.J., Mattiello, J., and LeBihan, D. (1994b). MR diffusion tensor spectroscopy and imaging. Biophys. J. *66*, 259–267.

Basser, P.J., Pajevic, S., Pierpaoli, C., Duda, J., and Aldroubi, A. (2000). In vivo fiber tractography using DT-MRI data. Magn. Reson. Med. *44*, 625–632.

Beaulieu, C. (2002). The basis of anisotropic water diffusion in the nervous system—a technical review. NMR Biomed. *15*, 438–455.

Bracewell, R.N. (1999). The Fourier Transform & Its Applications, 3rd edition (New York: McGraw-Hill).

Callaghan, P.T. (1993). Principles of Nuclear Magnetic Resonance Microscopy (Oxford: Oxford Press).

Callaghan, P.T. (1999). Rheo-NMR: nuclear magnetic resonance and the rheology of complex fluids. Rep. Prog. Phys. *62*, 599–670.

Callaghan, P.T., Eccles, C.D., and Xia, Y. (1988). NMR microscopy of dynamic displacements: k-space and q-space imaging. J. Phys. [E] *21*, 820–828.

Conturo, T.E., Lori, N.F., Cull, T.S., Akbudak, E., Snyder, A.Z., Shimony, J.S., McKinstry, R.C., Burton, H., and Raichle, M.E. (1999). Tracking neuronal fiber pathways in the living human brain. Proc. Natl. Acad. Sci. USA *96*, 10422–10427.

Cory, D.G., and Garroway, A.N. (1990). Measurement of translational displacement probabilities by NMR: an indicator of compartmentation. Magn. Reson. Med. *14*, 435–444.

Deans, S.R. (1993). The Radon Transform and Some of Its Applications (New York: Krieger).

de Boor, C. (2001). A Practical Guide to Splines Revised, 1st edition (New York: Springer Verlag).

Douek, P., Turner, R., Pekar, J., Patronas, N., and Le Bihan, D. (1991). MR color mapping of myelin fiber orientation. J. Comput. Assist. Tomogr. 15, 923–929.

Fasshauer, G.E., and Schumaker, L.L. (1998). Scattered data fitting on the sphere. In Mathematical Methods for Curves and Surfaces II, M. Daehlen, T. Lyche, and L.L. Schumaker, eds. (Nashville, TN: Vanderbilt University Press), pp. 117–166.

Fisher, N.I., Lewis, T., and Emgleton, B.J.J. (1987). Statistical Analysis of Spherical Data (Cambridge: Cambridge University).

Frank, L. (2001). Anisotropy in high angular resolution diffusion-weighted MRI. Magn. Reson. Med. 45, 935–939.

Frank, L.R. (2002). Characterization of anisotropy in high angular resolution diffusion-weighted MRI. Magn. Reson. Med. 47, 1083–1099.

Funk, P. (1916). Über eine geometrische Anwendung der Abelschen Integralgleichung. Math. Ann. 77, 129–135.

Hardy, R.L., and Nelson, S.A. (1986). A multiquadric-biharmonic represenation and approximation of disturbing potential. Geophys. Res. Lett. 13, 18–21.

Helgason, S. (1999). The Radon Transform, Volume 5 (Boston: Springer-Verlag).

Hoehn-Berlage, M., Eis, M., and Schmitz, B. (1999). Regional and directional anisotropy of apparent diffusion coefficient in rat brain. NMR Biomed. 12, 45–50.

Jones, D.K., Simmons, A., Williams, S.C., and Horsfield, M.A. (1999). Non-invasive assessment of axonal fiber connectivity in the human brain via diffusion tensor MRI. Magn. Reson. Med. 42, 37–41.

Kärger, J., and Heink, W. (1983). The propagator representation of molecular transport in microporous crystallites. J. Magn. Reson. 51, 1–7.

Kimmich, R., and Weber, H.W. (1993). NMR relaxation and the orientational structure factor. Phys. Rev. B 47, 11788–11794.

King, M.D., Houseman, J., Roussel, S.A., van Bruggen, N., Williams, S.R., and Gadian, D.G. (1994). q-space imaging of the brain. Magn. Reson. Med. 32, 707–713.

King, M.D., Houseman, J., Gadian, D.G., and Connelly, A. (1997). Localized q-space imaging of the mouse brain. Magn. Reson. Med. 38, 930–937.

Koch, M.A., Norris, D.G., and Hund-Georgiadis, M. (2002). An investigation of functional and anatomical connectivity using magnetic resonance imaging. Neuroimage 16, 241–250.

Kubicki, M., Westin, C.F., Maier, S.E., Mamata, H., Frumin, M., Ersner-Hershfield, H., Kikinis, R., Jolesz, F.A., McCarley, R., and Shenton, M.E. (2002). Diffusion tensor imaging and its application to neuropsychiatric disorders. Harv. Rev. Psychiatry 10, 324–326.

Kuchel, P.W., Durrant, C.J., Chapman, B.E., Jarrett, P.S., and Regan, D.G. (2000). Evidence of red cell alignment in the magnetic field of an NMR spectrometer based on the diffusion tensor of water. J. Magn. Reson. 145, 291–301.

Le Bihan, D., Turner, R., and Douek, P. (1993). Is water diffusion restricted in human brain white matter? An echo-planar NMR imaging study. Neuroreport 4, 887–890.

Lim, K.O., and Helpern, J.A. (2002). Neuropsychiatric applications of DTI—a review. NMR Biomed. 15, 587–593.

Mangin, J.F., Poupon, C., Cointepas, Y., Riviere, D., Papadopoulos-Orfanos, D., Clark, C.A., Regis, J., and Le Bihan, D. (2002). A framework based on spin glass models for the inference of anatomical connectivity from diffusion-weighted MR data—a technical review. NMR Biomed. 25, 481–492.

Mardia, K.V., and Jupp, P.E. (2000). Directional Statistics (Chichester: John Wiley & Sons).

McKinstry, R.C., Mathur, A., Miller, J.H., Ozcan, A., Snyder, A.Z., Schefft, G.L., Almli, C.R., Shiran, S.I., Conturo, T.E., and Neil, J.J. (2002). Radial organization of developing preterm human cerebral

cortex revealed by non-invasive water diffusion anisotropy MRI. Cereb. Cortex 12, 1237–1243.

Mori, S., and Van Zijl, P.C. (2002). Fiber tracking: principles and strategies—a technical review. NMR Biomed. 15, 468–480.

Mori, S., Crain, B.J., Chacko, V.P., and van Zijl, P.C. (1999). Three-dimensional tracking of axonal projections in the brain by magnetic resonance imaging. Ann. Neurol. 45, 265–269.

Mugler, J.P., III, and Brookeman, J.R. (1990). Three-dimensional magnetization-prepared rapid gradient-echo imaging (3D MPRAGE). Magn. Reson. Med. 15, 152–157.

Niewenhuys, R. (1996). The Human Central Nervous System: A Synopsis and Atlas, 3 edition (New York: Springer Verlag).

Norris, D.G. (2001). The effects of microscopic tissue parameters on the diffusion weighted magnetic resonance imaging experiment. NMR Biomed. 14, 77–93.

Parker, G.J., Stephan, K.E., Barker, G.J., Rowe, J.B., MacManus, D.G., Wheeler-Kingshott, C.A., Ciccarelli, O., Passingham, R.E., Spinks, R.L., Lemon, R.N., and Turner, R. (2002). Initial demonstration of in vivo tracing of axonal projections in the macaque brain and comparison with the human brain using diffusion tensor imaging and fast marching tractography. Neuroimage 15, 797–809.

Pierpaoli, C., Jezzard, P., Basser, P.J., Barnett, A., and Di Chiro, G. (1996). Diffusion tensor MR imaging of the human brain. Radiology 201, 637–648.

Pierpaoli, C., Barnett, A., Pajevic, S., Chen, R., Penix, L.R., Virta, A., and Basser, P. (2001). Water diffusion changes in Wallerian degeneration and their dependence on white matter architecture. Neuroimage 13, 1174–1185.

Poupon, C., Clark, C.A., Frouin, V., Regis, J., Bloch, I., Le Bihan, D., and Mangin, J. (2000). Regularization of diffusion-based direction maps for the tracking of brain white matter fascicles. Neuroimage 12, 184–195.

Reese, T.G., Weisskoff, R.M., Smith, R.N., Rosen, B.R., Dinsmore, R.E., and Wedeen, V.J. (1995). Imaging myocardial fiber architecture in vivo with magnetic resonance. Magn. Reson. Med. 34, 786–791.

Reese, T.G., Heid, O., Weisskoff, R.M., and Wedeen, V.J. (2003). Reduction of eddy-current-induced distortion in diffusion MRI using a twice-refocused spin echo. Magn. Reson. Med. 49, 177–182.

Stejskal, E.O., and Tanner, J.E. (1965). Spin diffusion measurements: spin echoes in the presence of a time-dependent field gradient. J. Chem. Phys. 42, 288–292.

Thornton, J.S., Ordidge, R.J., Penrice, J., Cady, E.B., Amess, P.N., Punwani, S., Clemence, M., and Wyatt, J.S. (1997). Anisotropic water diffusion in white and gray matter of the neonatal piglet brain before and after transient hypoxia-ischaemia. Magn. Reson. Imaging 15, 433–440.

Tuch, D.S. (2002). Diffusion MRI of complex tissue structure. PhD thesis, Harvard University-Massachusetts Institute of Technology, Cambridge, Massachusetts.

Tuch, D.S., Wedeen, V.J., Dale, A.M., George, J.S., and Belliveau, J.W. (2001). Conductivity tensor mapping of the human brain using diffusion tensor MRI. Proc. Natl. Acad. Sci. USA 98, 11697–11701.

Tuch, D.S., Reese, T.G., Wiegell, M.R., Makris, N., Belliveau, J.W., and Wedeen, V.J. (2002). High angular resolution diffusion imaging reveals intravoxel white matter fiber heterogeneity. Magn. Reson. Med. 48, 577–582.

Turner, R., and Le Bihan, D. (1990). Single-shot diffusion imaging at 2.0 Tesla. J. Magn. Reson. 86, 445–452.

Wiegell, M.R., Larsson, H.B., and Wedeen, V.J. (2000). Fiber crossing in human brain depicted with diffusion tensor MR imaging. Radiology 217, 897–903.

Xue, R., van Zijl, P.C., Crain, B.J., Solaiyappan, M., and Mori, S. (1999). In vivo three-dimensional reconstruction of rat brain axonal

projections by diffusion tensor imaging. Magn. Reson. Med. *42*, 1123–1127.

Zavada, T., and Kimmich, R. (1999). Surface fractals probed by adsorbate spin-lattice relaxation dispersion. Phys. Rev. E Stat. Phys. Plasmas. Fluids Relat. Interdiscip. Topics *59*, 5848–5854.

Zavada, T., Sudland, N., Kimmich, R., and Nonnenmacher, T.F. (1999). Propagator representation of anomalous diffusion: the orientational structure factor formalism in NMR. Phys. Rev. E Stat. Phys. Plasmas. Fluids Relat. Interdiscip. Topics *60*, 1292–1298.